Discontinuous Hamiltonian Finite Element Method for Bilinear Poisson Brackets

Yan Xu*, Jaap J.W. van der Vegt† and Onno Bokhove‡

Department of Applied Mathematics, University of Twente

P.O. Box 217, 7500 AE, Enschede, The Netherlands

October 19, 2007

Abstract

We develop a Hamiltonian discontinuous finite element discretization of a generalized Hamiltonian system for linear hyperbolic systems, which includes the rotating shallow water equations, the acoustic and Maxwell equations. These equations have a Hamiltonian structure with a bilinear Poisson bracket, and as a consequence the phase-space structure, mass and energy are preserved. We discretize the bilinear Poisson bracket in each element with discontinuous elements and introduce numerical fluxes via integration by parts while preserving the skew-symmetry of the bracket. This automatically results in a mass and energy conservative discretization when combined with a symplectic time integration method. For comparison, the discontinuous Galerkin method for this problem is also used. A variety of numerical examples is shown to illustrate the accuracy and capability of the new method.

*Current address: Department of Mathematics, University of Science and Technology of China, Hefei, Anhui 230026, P.R. China, email yxu@ustc.edu.cn. Research supported by NSFC grant 10601055.

†E-mail: j.j.w.vandervegt@math.utwente.nl

‡Corresponding author, e-mail: o.bokhove@math.utwente.nl

AMS subject classification: 65M60, 76M10

Key words: rotating shallow water equations, acoustic equations, Maxwell equations, Hamiltonian dynamics, discontinuous Galerkin method, numerical flux

1 Introduction

Many space-time dynamical systems in physics and mathematics are Hamiltonian and have conservation laws associated with their Hamiltonian formulation. Preservation of the Hamiltonian formulation in the discretizations of these systems is especially desirable in long-time predictions where conservation laws constrain the dynamics whereas dissipative discretizations do not. A space-time Hamiltonian system consists of the dynamics of an arbitrary functional of the variables, a (generalized) Poisson bracket and a Hamiltonian, see e.g. [12]. This (generalized) Poisson bracket is skew-symmetric and satisfies the Jacobi identity [11]. Typically the formulation deals with functionals. Here, we restrict attention to a generalized Hamiltonian formulation for linear hyperbolic systems including the rotating linearized shallow water equations, the acoustic and Maxwell's equations. These linear hyperbolic equations generally involve given functions of space, representing the spatial variation of material properties of the associated physical system.

The Hamiltonian formulation of our generalized system guarantees that energy, mass and phase-space structure are preserved. The standard discontinuous Galerkin finite element method, however, fails to conserve energy when the material properties are spatially varying, while discrete energy conservation has been obtained for constant coefficients [14]. This motivated us to derive a weak formulation and corresponding discontinuous finite element discretization directly based on discretizing the generalized Poisson bracket in the Hamiltonian formulation. Since this results in a skew-symmetric spatial discretization, energy conservation is directly ensured. In addition, mass is conserved. By additional use of symplectic splitting methods for the time discretization, the phase space structure is preserved while the energy oscillates weakly around its initial value [5].

To investigate the strength of our Hamiltonian discontinuous finite element formulation we

contrast it with the classical discontinuous Galerkin (DG) formulation involving an alternating numerical flux [14]. This classical DG method is a class of finite element methods using completely discontinuous piecewise polynomial spaces for the numerical solution and the test functions in the spatial variables, usually coupled with an explicit and nonlinearly stable high order Runge-Kutta time discretization [13], first developed in [3, 4].

The standard DG finite element method with an alternating numerical flux and our new DG finite element method based on the skew-symmetric Hamiltonian formulation coincide when the material functions are constant. It demonstrates that the alternating flux can be interpreted as a skew-symmetric Hamiltonian flux. In contrast, the skew-symmetric flux becomes essential to conserve energy and phase space volume in the important case of spatially varying material functions.

The outline of our article is as follows. In Section 2, we present the generalized linear hyperbolic system and its Hamiltonian formulation. In Section 3, we derive the discontinuous finite element discretization for the generalized linear hyperbolic equations and the ensuing discrete skew-symmetric bilinear bracket. For comparison, we also give the DG method for the generalized linear hyperbolic equations. The symplectic splitting method and classical Runge-Kutta time discretizations used are presented in Section 4. Section 5 contains numerical results for the nonlinear problems to demonstrate the accuracy and capabilities of the new method. Concluding remarks are given in Section 6.

2 Hamiltonian formulation

2.1 General formulation

We consider the linear hyperbolic system of equations

$$\frac{\partial \boldsymbol{v}}{\partial t} + \boldsymbol{\mathcal{D}}(C\,\eta) + f\,\boldsymbol{v}^{\perp} = 0, \tag{2.1}$$

$$\frac{\partial \eta}{\partial t} + \boldsymbol{\mathcal{D}}\cdot(B\,\boldsymbol{v}) = 0, \quad \forall (x,y) \in \Omega \subseteq \mathbb{R}^2, \tag{2.2}$$

with as variables the two-dimensional vector field $\boldsymbol{v} = \boldsymbol{v}(x,y,t) = (u,v)^T$, $\boldsymbol{v}^\perp = (-v,u)^T$ and the scalar function $\eta = \eta(x,y,t)$ depending on spatial coordinates x, y and time t; and, the given functions $B = B(x,y) > 0$, $C = C(x,y) > 0$ and $f = f(x,y)$. The operator $\boldsymbol{\mathcal{D}}$ is either the differential operator $\nabla = (\frac{\partial}{\partial x}, \frac{\partial}{\partial y})^T$, or $-\nabla^\perp = (\frac{\partial}{\partial y}, -\frac{\partial}{\partial x})^T$.

The domain Ω has a boundary $\partial\Omega$, which is subdivided into boundary segments, at which boundary conditions are specified, such as periodic boundary conditions and/or solid walls. At solid walls $\partial\Omega_s \subseteq \partial\Omega$ the boundary condition

$$\boldsymbol{\mathcal{N}} \cdot \boldsymbol{v} = 0 \tag{2.3}$$

is imposed. Here the vector $\boldsymbol{\mathcal{N}}$ is either the normal vector $\boldsymbol{n} = (n_x, n_y)^T$ or the tangential vector $\boldsymbol{n}^\perp = (n_y, -n_x)^T$ at the boundary of $\partial\Omega_s$, depending if the differential operator $\boldsymbol{\mathcal{D}}$ is equal to $\boldsymbol{\mathcal{D}} = \nabla$ or $\boldsymbol{\mathcal{D}} = -\nabla^\perp$, respectively. The system (2.1)-(2.2) is completed with the initial conditions $\boldsymbol{v}(x,y,0) = \boldsymbol{v}_0(x,y)$ and $\eta(x,y,0) = \eta_0(x,y)$. Additional consistency requirements emerge because (2.3) must be preserved in time.

The linear system of equations (2.1)-(2.2) has a Hamiltonian formulation, see e.g. [1], which can be expressed using the Poisson bracket $\{\cdot,\cdot\}_1$ as

$$\frac{\mathrm{d}\mathcal{F}}{\mathrm{d}t} = \{\mathcal{F},\mathcal{H}\}_1 = \int_\Omega \left(\frac{f}{B} \frac{\delta \mathcal{F}^\perp}{\delta \boldsymbol{v}} \cdot \frac{\delta \mathcal{H}}{\delta \boldsymbol{v}} + \left(\boldsymbol{\mathcal{D}} \cdot \frac{\delta \mathcal{F}}{\delta \boldsymbol{v}} \right) \frac{\delta \mathcal{H}}{\delta \eta} - \frac{\delta \mathcal{F}}{\delta \eta} \left(\boldsymbol{\mathcal{D}} \cdot \frac{\delta \mathcal{H}}{\delta \boldsymbol{v}} \right) \right) \mathrm{d}\Omega \tag{2.4}$$

with Hamiltonian

$$\mathcal{H} = \int_\Omega \left(\frac{1}{2} B \, |\boldsymbol{v}|^2 + \frac{1}{2} C \, \eta^2 \right) \mathrm{d}\Omega. \tag{2.5}$$

The functional derivatives of the Hamiltonian are defined as

$$\delta\mathcal{H} := \lim_{\epsilon \to 0} \frac{\mathcal{H}[\boldsymbol{v} + \epsilon\delta\boldsymbol{v}, \eta + \epsilon\delta\eta] - \mathcal{H}[\boldsymbol{v},\eta]}{\epsilon} := \int_\Omega \left(\frac{\delta \mathcal{H}}{\delta \boldsymbol{v}} \cdot \delta\boldsymbol{v} + \frac{\delta \mathcal{H}}{\delta \eta} \delta\eta \right) \mathrm{d}\Omega. \tag{2.6}$$

Hence, it follows from (2.5) and (2.6) that

$$\delta\mathcal{H} = \int_\Omega \left(B \, \boldsymbol{v} \cdot \delta\boldsymbol{v} + C\eta \, \delta\eta \right) \mathrm{d}\Omega \tag{2.7}$$

and by using (2.6) with (2.7) we obtain the functional derivatives

$$\frac{\delta \mathcal{H}}{\delta \boldsymbol{v}} = B\boldsymbol{v} \quad \text{and} \quad \frac{\delta \mathcal{H}}{\delta \eta} = C\eta. \tag{2.8}$$

The equations for the velocity field $\boldsymbol{v}$, given by (2.1), are obtained if we choose the functional $\mathcal{F}$ in (2.4) as:

$$\mathcal{F}[\boldsymbol{v}] = \int_\Omega \boldsymbol{w_v}(\boldsymbol{x}) \cdot \boldsymbol{v}(\boldsymbol{x}, t)\, d\Omega,$$

with $\boldsymbol{w_v}$ arbitrary functions which satisfy the condition $\boldsymbol{\mathcal{N}} \cdot \boldsymbol{w_v} = 0$ at $\partial\Omega_s$. Similarly, the equation for η, given by (2.2), is obtained if we choose the functional $\mathcal{F}$ with w_η arbitrary functions as

$$\mathcal{F}[\eta] = \int_\Omega w_\eta(\boldsymbol{x})\eta(\boldsymbol{x}, t)\, d\Omega.$$

The bracket $\{\mathcal{F}, \mathcal{H}\}_1$ is seen to be skew-symmetric and also satisfies the Jacobi identity

$$\{\mathcal{K}, \{\mathcal{F}, \mathcal{G}\}_1\}_1 + \{\mathcal{F}, \{\mathcal{G}, \mathcal{K}\}_1\}_1 + \{\mathcal{G}, \{\mathcal{K}, \mathcal{F}\}_1\}_1 = 0, \tag{2.9}$$

for arbitrary functionals $\mathcal{F}, \mathcal{G}$ and $\mathcal{K}$. The skew-symmetry of the bracket in (2.4) guarantees energy conservation, since

$$\frac{\mathrm{d}\mathcal{H}}{\mathrm{d}t} = \{\mathcal{H}, \mathcal{H}\}_1 = 0,$$

and mass conservation follows likewise

$$\frac{\mathrm{d}\mathcal{M}}{\mathrm{d}t} = \{\mathcal{M}, \mathcal{H}\}_1 = 0 \qquad \text{with} \qquad \mathcal{M} = \int_\Omega \eta \,\mathrm{d}\Omega.$$

An alternative form of bracket $\{\cdot, \cdot\}_1$ appears after integration by parts and using the boundary conditions, i.e.

$$\frac{\mathrm{d}\mathcal{F}}{\mathrm{d}t} = \{\mathcal{F}, \mathcal{H}\}_2 := \int_\Omega \left(\frac{f}{B} \frac{\delta \mathcal{F}}{\delta \boldsymbol{v}}^\perp \cdot \frac{\delta \mathcal{H}}{\delta \boldsymbol{v}} - \frac{\delta \mathcal{F}}{\delta \boldsymbol{v}} \cdot \left(\boldsymbol{\mathcal{D}} \frac{\delta \mathcal{H}}{\delta \eta} \right) - \frac{\delta \mathcal{F}}{\delta \eta} \left(\boldsymbol{\mathcal{D}} \cdot \frac{\delta \mathcal{H}}{\delta \boldsymbol{v}} \right) \right) \mathrm{d}\Omega. \tag{2.10}$$

The natural boundary conditions for $\boldsymbol{v}$ at solid walls extend to the functional derivatives; they are for arbitrary $\mathcal{F}$

$$\boldsymbol{\mathcal{N}} \cdot \frac{\delta \mathcal{F}}{\delta \boldsymbol{v}} = 0. \tag{2.11}$$

The skew-symmetric nature is now hidden in (2.10) in contrast to the form of the bracket (2.4).

Although $\{\cdot, \cdot\}_1$ directly results in a skew-symmetric discrete bracket it does not directly show a relation to the classical DG method, which is based on a weak formulation of the partial differential equations, cf. [4]. This is more clear if we use the discrete form of $\{\cdot, \cdot\}_2$, see Section 3. In particular, we will show that for certain numerical fluxes the spatial discretization of both brackets coincides, and then both approaches guarantee discrete energy conservation.

2.2 Applications

In this section, we will discuss several important examples of bilinear Poisson brackets which can be discretized with the Hamiltonian discontinuous finite element discretization derived later.

2.2.1 Rotating shallow water equations

The linear rotating shallow water equations are a special case of system (2.2) with $\boldsymbol{\mathcal{D}} = \nabla$, $B(x,y) = D(x,y)$ the given rest depth, $C(x,y) = g$ the constant gravitational acceleration, and $f = f(x,y)$ the given Coriolis parameter. Hence, the resulting rotating shallow water equations are

$$\frac{\partial \boldsymbol{v}}{\partial t} + \boldsymbol{\nabla}(g\,\eta) + f\,\boldsymbol{v}^{\perp} = 0, \qquad \frac{\partial \eta}{\partial t} + \boldsymbol{\nabla}\cdot(D\,\boldsymbol{v}) = 0, \tag{2.12}$$

where $\boldsymbol{v}$ is the velocity and η is the water depth. Slip flow implies no flow through solid walls: $\boldsymbol{n}\cdot\boldsymbol{v} = 0$, and when $f \neq 0$ geostrophic balance holds at these solid boundaries, $\boldsymbol{n}\cdot\boldsymbol{\nabla}(g\,\eta) + f\,\boldsymbol{n}\cdot\boldsymbol{v}^{\perp} = 0$, such that the flow tangential to the wall is balanced by the normal gradient of the geopotential $g\,\eta$. When $f = 0$ the usual Neuman relation $\boldsymbol{n}\cdot\boldsymbol{\nabla}\eta = 0$ at a solid-wall boundary results.

The linear rotating shallow water equations have the following Hamiltonian formulation

$$\frac{\mathrm{d}\mathcal{F}}{\mathrm{d}t} = \{\mathcal{F}, \mathcal{H}_l\}_1 = \int_\Omega \left(\frac{f}{D} \frac{\delta \mathcal{F}}{\delta \boldsymbol{v}}^{\perp} \cdot \frac{\delta \mathcal{H}_l}{\delta \boldsymbol{v}} + \left(\boldsymbol{\nabla}\cdot \frac{\delta \mathcal{F}}{\delta \boldsymbol{v}} \right) \frac{\delta \mathcal{H}_l}{\delta \eta} - \frac{\delta \mathcal{F}}{\delta \eta} \left(\boldsymbol{\nabla}\cdot \frac{\delta \mathcal{H}_l}{\delta \boldsymbol{v}} \right) \right) \mathrm{d}\Omega, \tag{2.13}$$

with Hamiltonian

$$\mathcal{H}_l = \int_\Omega \left(\frac{1}{2}\, D\, |\boldsymbol{v}|^2 + \frac{1}{2}\, g\, \eta^2 \right) \mathrm{d}\Omega. \tag{2.14}$$

Its functional derivatives are

$$\frac{\delta \mathcal{H}_l}{\delta \boldsymbol{v}} = D\boldsymbol{v} \quad \text{and} \quad \frac{\delta \mathcal{H}_l}{\delta \eta} = g\eta. \tag{2.15}$$

2.2.2 2D Maxwell equations

Another application of equation (2.2) concerns the two-dimensional Maxwell equations with $\boldsymbol{v} = \boldsymbol{H} = (H_x, H_y)^T$ the magnetic field, $\eta = E_z$ the electric field, and $\boldsymbol{\mathcal{D}} = -\nabla^{\perp}$, $C = \mu^{-1}$,

$B = \epsilon^{-1}$ and $f = 0$. The two-dimensional Maxwell equations are defined as

$$\frac{\partial \boldsymbol{H}}{\partial t} = \boldsymbol{\nabla}^{\perp}(\mu^{-1} E_z), \qquad \frac{\partial E_z}{\partial t} = \boldsymbol{\nabla}^{\perp} \cdot (\epsilon^{-1} \boldsymbol{H}), \tag{2.16}$$

where μ is the magnetic permeability and ϵ is the dielectric permittivity. At solid walls $\boldsymbol{n} \cdot \boldsymbol{H}^{\perp} = 0$.

The Maxwell equations have the following Hamiltonian formulation

$$\frac{\mathrm{d}\mathcal{F}}{\mathrm{d}t} = \{\mathcal{F}, \mathcal{H}_m\}_1 = \int_{\Omega} \left(- \left(\boldsymbol{\nabla}^{\perp} \cdot \frac{\delta \mathcal{F}}{\delta \boldsymbol{H}} \right) \frac{\delta \mathcal{H}_m}{\delta E_z} + \frac{\delta \mathcal{F}}{\delta E_z} \left(\boldsymbol{\nabla}^{\perp} \cdot \frac{\delta \mathcal{H}_m}{\delta \boldsymbol{H}} \right) \right) \mathrm{d}\Omega, \tag{2.17}$$

with Hamiltonian

$$\mathcal{H}_m = \int_{\Omega} \left(\frac{1}{2} \epsilon^{-1} |\boldsymbol{H}|^2 + \frac{1}{2} \mu^{-1} E_z^2 \right) \mathrm{d}\Omega. \tag{2.18}$$

Its functional derivatives are

$$\frac{\delta \mathcal{H}_m}{\delta \boldsymbol{H}} = \epsilon^{-1} \boldsymbol{H} \quad \text{and} \quad \frac{\delta \mathcal{H}_m}{\delta E_z} = \mu^{-1} E_z. \tag{2.19}$$

2.2.3 Acoustic equations

The two-dimensional acoustic equations [9] arise from (2.2) when $\boldsymbol{v} = (u, v)^T$ is taken as the velocity field, $\eta = \rho$ as density, and $\boldsymbol{\mathcal{D}} = \nabla$, $C = c_0^2/\rho_0$ with $B = \rho_0$ as reference density, and $f = 0$. The two-dimensional acoustic equations then become

$$\frac{\partial \boldsymbol{v}}{\partial t} + \boldsymbol{\nabla} \left(\frac{c_0^2}{\rho_0} \rho \right) = 0, \qquad \frac{\partial \rho}{\partial t} + \boldsymbol{\nabla} \cdot (\rho_0 \, \boldsymbol{v}) = 0. \tag{2.20}$$

Slip flow again implies no flow through solid walls: $\boldsymbol{n} \cdot \boldsymbol{v} = 0$. The acoustic equations have the following Hamiltonian formulation

$$\frac{\mathrm{d}\mathcal{F}}{\mathrm{d}t} = \{\mathcal{F}, \mathcal{H}_a\}_1 = \int_{\Omega} \left(\left(\boldsymbol{\nabla} \cdot \frac{\delta \mathcal{F}}{\delta \boldsymbol{v}} \right) \frac{\delta \mathcal{H}_a}{\delta \rho} - \frac{\delta \mathcal{F}}{\delta \rho} \left(\boldsymbol{\nabla} \cdot \frac{\delta \mathcal{H}_a}{\delta \boldsymbol{v}} \right) \right) \mathrm{d}\Omega, \tag{2.21}$$

with Hamiltonian

$$\mathcal{H}_a = \int_{\Omega} \left(\frac{1}{2} \rho_0 |\boldsymbol{v}|^2 + \frac{1}{2} \frac{c_0^2}{\rho_0} \rho^2 \right) \mathrm{d}\Omega, \tag{2.22}$$

and functional derivatives

$$\frac{\delta \mathcal{H}_a}{\delta \boldsymbol{v}} = \rho_0 \boldsymbol{v} \quad \text{and} \quad \frac{\delta \mathcal{H}_a}{\delta \rho} = \frac{c_0^2}{\rho_0} \rho. \tag{2.23}$$

3 Discrete Hamiltonian formulation

In this section, we will derive a spatial Hamiltonian discontinuous finite element discretization for the Hamiltonian system (2.4) and (2.5). It thus guarantees conservation of energy and phase space volume by default. It will be shown that it coincides with a particular discretization of (2.10) with Hamiltonian (2.5). For comparison, we will also give the DG discretization for the generalized linear hyperbolic equations (2.1) and (2.2).

3.1 Notation

Let $\mathcal{T}_h$ denote a tessellation of Ω with shape-regular elements K. Let Γ denote the set of all edges in the tessellation $\mathcal{T}_h$, with Γ_i the set of interior edges and Γ_b the set of edges at the domain boundary.

In order to describe the flux functions we need to introduce some notation. Let e be an edge shared by the "left" and "right" elements K_L and K_R. Define the normal vectors n_L and n_R on e pointing exterior to K_L and K_R, respectively. When e lies on the domain boundary, we adopt the convention that K_L lies inside Ω. If ψ is a function on K_L and K_R, but possibly discontinuous across e, let $\psi_L = (\psi|_{K_L})|_e$ and $\psi_R = (\psi|_{K_R})|_e$ denote the left and right trace, respectively.

Let $\mathcal{P}^p(K)$ be the space of polynomials of degree at most p on $K \in \mathcal{T}_h$, with $p \geq 0$. The finite element spaces V_h and W_h are denoted by

$$V_h = \{\psi \in L^2(\Omega) : \quad \psi|_K \in \mathcal{P}^p(K) \quad \forall K \in \mathcal{T}_h\},$$
$$W_h = \{\boldsymbol{\psi} \in \big(L^2(\Omega)\big)^2 : \quad \boldsymbol{\psi}|_K \in (\mathcal{P}^p(K))^2 \quad \forall K \in \mathcal{T}_h,\ \boldsymbol{\mathcal{N}} \cdot \boldsymbol{\psi}|_{\partial\Omega_s} = 0\}.$$

The number of degrees of freedom on an element is denoted by $N_K = \dim\big(\mathcal{P}^p(K)\big)$.

3.2 Discrete Hamiltonian formulation and variational derivatives

Consider the linear system (2.1)-(2.2), rewritten in the form

$$\frac{\partial \boldsymbol{v}}{\partial t} + \boldsymbol{\mathcal{D}}\, r + \frac{f}{B}\, \mathbf{Q}^{\perp} = 0 \qquad \text{and} \qquad \frac{\partial \eta}{\partial t} + \boldsymbol{\mathcal{D}} \cdot \mathbf{Q} = 0 \tag{3.1}$$

with $\mathbf{Q} = B\boldsymbol{v}$ and $r = C\eta$. Energy conservation follows by multiplying the first equation by $\mathbf{Q}$ and the second equation by r, integration over the domain Ω, applying Gauss' law and using the boundary conditions, i.e.

$$\frac{\mathrm{d}}{\mathrm{d}t}\frac{1}{2}\int_\Omega B|\boldsymbol{v}|^2 + C\,\eta^2 \mathrm{d}\Omega = -\int_\Omega \boldsymbol{\mathcal{D}}\cdot(\mathbf{Q}\,r)\mathrm{d}\Omega = 0. \tag{3.2}$$

The crucial point in a corresponding discontinuous Hamiltonian discretization is to consider $\mathbf{Q}$ and r as additional variables, linked to $B\boldsymbol{v}$ and $C\eta$ via a projection onto the finite element space.

The Hamiltonian discretization automatically does this because $\mathbf{Q}_h = \delta H/\delta \boldsymbol{v}_h$ and $r_h = \delta H/\delta \eta_h$. Consequently, we should use $\mathbf{Q}_h$ and r_h in the discretization and not $B_h\mathbf{v}_h$ and $C_h\eta_h$ as the former lie in $V_h \times V_h$ and V_h, respectively, while the latter do not. We will show that in this way the Hamiltonian formalism projects the functional derivatives onto the Galerkin space and that the Hamiltonian remains positive.

In the discrete Hamiltonian formulation we will use H to denote the discrete approximation of $\mathcal{H}$. The discrete Hamiltonian is

$$H = \frac{1}{2}\sum_K \int_K \left(B_h\,|\boldsymbol{v}_h|^2 + C_h\,\eta_h^2\right)\,\mathrm{d}\Omega, \tag{3.3}$$

and the variational derivatives are not equal in the strong sense but only in a weak sense

$$\frac{\delta H}{\delta \boldsymbol{v}_h} = \mathbf{Q}_h \neq B_h\,\boldsymbol{v}_h, \quad \frac{\delta H}{\delta \eta_h} = r_h \neq C_h\,\eta_h, \tag{3.4}$$

where B_h, C_h, r_h, $\eta_h \in V_h$ and $\boldsymbol{v}_h, \mathbf{Q}_h \in V_h \times V_h$.

For the discretization of the velocity equations (2.1) we consider the functional $F[\boldsymbol{v}_h] = \int_\Omega \boldsymbol{v}_h \cdot \boldsymbol{\psi}\,\mathrm{d}\Omega$, with $\boldsymbol{\psi} \in W_h$ arbitrary test functions. Using the definition of the functional derivatives

$$\delta F := \lim_{\epsilon\to 0}\frac{F[\boldsymbol{v}_h + \epsilon\delta\boldsymbol{v}_h] - F[\boldsymbol{v}_h]}{\epsilon} = \int_\Omega \boldsymbol{\psi}\cdot\delta\boldsymbol{v}_h\,\mathrm{d}\Omega, \tag{3.5}$$

we obtain

$$\frac{\delta F}{\delta \boldsymbol{v}_h} = \boldsymbol{\psi}. \tag{3.6}$$

The test function $\boldsymbol{\psi}$ is taken from the space W_h and not from $V_h \times V_h$, since the functional derivative of $F[\boldsymbol{v}_h]$ must satisfy the condition (2.11) at the boundary Ω_s. This implies that

$$\boldsymbol{\mathcal{N}} \cdot \frac{\delta F}{\delta \boldsymbol{v}_h} = \boldsymbol{\mathcal{N}} \cdot \boldsymbol{\psi} = 0. \tag{3.7}$$

Hence the test functions $\boldsymbol{\psi}$ at the domain boundary must have either a zero normal or tangential component depending on the choice of the operator $\boldsymbol{\mathcal{D}}$, viz. $\boldsymbol{\mathcal{D}} = \nabla$ or $\boldsymbol{\mathcal{D}} = -\nabla^{\perp}$.

Likewise, for the discretization of the equation for η, given by (2.2), we set the functional F equal to $F[\eta_h] = \int_\Omega \eta_h \phi \, \mathrm{d}\Omega$, with $\phi \in V_h$ arbitrary test functions, and we obtain the functional derivative

$$\frac{\delta F}{\delta \eta_h} = \phi. \tag{3.8}$$

3.3 The discontinuous Hamiltonian formulation

In this section we will derive a discrete formulation for the Hamiltonian system (2.4)-(2.5). We will start with bracket $\{\cdot,\cdot\}_2$, defined in (2.10), and by choosing proper numerical fluxes we can demonstrate the skew symmetry of the discrete bracket when using discontinuous basis functions. This then automatically implies conservation of mass and energy at the discrete level. The discrete form of formulation (2.10) is obtained by introducing the tessellation $\mathcal{T}_h$ of Ω and the discrete approximations of the functionals $\mathcal{F}$ and $\mathcal{H}$. After integration by parts over each element $K \in \mathcal{T}_h$, we obtain

$$\begin{aligned}
\frac{\mathrm{d}F}{\mathrm{d}t} = \{F, H\}_2 = &\sum_{K\in\mathcal{T}_h} \int_K \left(\frac{f_h}{B_h} \frac{\delta F}{\delta \boldsymbol{v}_h}^{\perp} \cdot \frac{\delta H}{\delta \boldsymbol{v}_h} \right) \mathrm{d}\Omega \\
&+ \sum_{K\in\mathcal{T}_h} \int_K \left(\left(\boldsymbol{\mathcal{D}} \cdot \frac{\delta F}{\delta \boldsymbol{v}_h} \right) \frac{\delta H}{\delta \eta_h} + \left(\boldsymbol{\mathcal{D}} \frac{\delta F}{\delta \eta_h} \right) \cdot \frac{\delta H}{\delta \boldsymbol{v}_h} \right) \mathrm{d}\Omega \\
&- \sum_{K\in\mathcal{T}_h} \int_{\partial K} \left(\boldsymbol{\mathcal{N}} \cdot \frac{\delta F}{\delta \boldsymbol{v}_h} \widehat{\frac{\delta H}{\delta \eta_h}} + \widehat{\boldsymbol{\mathcal{N}} \cdot \frac{\delta H}{\delta \boldsymbol{v}_h}} \frac{\delta F}{\delta \eta_h} \right) dS,
\end{aligned} \tag{3.9}$$

where the numerical fluxes $\widehat{\frac{\delta H}{\delta \eta_h}}$ and $\widehat{\boldsymbol{\mathcal{N}} \cdot \frac{\delta H}{\delta \boldsymbol{v}_h}}$ are introduced to account for the multi-valued traces of $\frac{\delta H}{\delta \eta_h}$ and $\boldsymbol{\mathcal{N}} \cdot \frac{\delta H}{\delta \boldsymbol{v}_h}$ at the element boundaries ∂K. Since all derivative terms in the Poisson bracket $\{\cdot,\cdot\}_2$ are on the Hamilton functional, the numerical flux at the element boundaries can

be chosen using the alternating numerical flux proposed in [14]. This procedure is not obvious for the Poisson bracket $\{\cdot,\cdot\}_1$, (2.4), because the functional derivatives of F, (3.6) and (3.8), are arbitrary test functions.

By choosing the functional F alternatively as

$$\int_\Omega \boldsymbol{v}_h \cdot \boldsymbol{\psi}\,\mathrm{d}\Omega \quad \text{and} \quad \int_\Omega \eta_h \phi\,\mathrm{d}\Omega,$$

introducing these relations into (3.9) and using the discrete variational derivatives (3.4), (3.6) and (3.8), the discrete formulation for (2.1)-(2.2) emerges:

Find a $\boldsymbol{v}_h \in V_h \times V_h$ and $\eta_h \in V_h$, such that for all $\boldsymbol{\psi} \in W_h$ and $\phi \in V_h$ the following relation is satisfied:

$$\int_K \frac{\partial \boldsymbol{v}_h}{\partial t} \cdot \boldsymbol{\psi}\mathrm{d}\Omega = \int_K \left(-\frac{f_h}{B_h}\mathbf{Q}_h^\perp \cdot \boldsymbol{\psi} + r_h \boldsymbol{\mathcal{D}} \cdot \boldsymbol{\psi} \right) \mathrm{d}\Omega - \int_{\partial K} \widehat{r_h}\boldsymbol{\mathcal{N}} \cdot \boldsymbol{\psi}\mathrm{d}S, \tag{3.10}$$

$$\int_K \frac{\partial \eta_h}{\partial t}\phi\mathrm{d}\Omega = \int_K \mathbf{Q}_h \cdot \boldsymbol{\mathcal{D}}\phi\,\mathrm{d}\Omega - \int_{\partial K} \widehat{\boldsymbol{\mathcal{N}}\cdot\mathbf{Q}_h}\phi\,\mathrm{d}S, \tag{3.11}$$

where $\mathbf{Q}_h \in V_h \times V_h$ and $r_h \in V_h$ are obtained from the relations

$$\int_K \mathbf{Q}_h \cdot \boldsymbol{\phi}\mathrm{d}\Omega = \int_K B_h \boldsymbol{v}_h \cdot \boldsymbol{\phi}\mathrm{d}\Omega, \quad \forall \boldsymbol{\phi} \in V_h \times V_h, \tag{3.12}$$

$$\int_K r_h \phi \mathrm{d}x\mathrm{d}y = \int_K C_h \eta_h \phi \mathrm{d}\Omega, \qquad \forall \phi \in V_h. \tag{3.13}$$

We choose the following alternating numerical fluxes at edges $e \in \Gamma_i$

$$\begin{aligned} \widehat{\frac{\delta H}{\delta \eta_h}} &= \widehat{r_h} = \theta \frac{\delta H}{\delta \eta_h^L} + (1-\theta)\frac{\delta H}{\delta \eta_h^R}, \\ \widehat{\boldsymbol{\mathcal{N}}\cdot\frac{\delta H}{\delta \boldsymbol{v}_h}} &= \widehat{\boldsymbol{\mathcal{N}}\cdot\mathbf{Q}_h} = (1-\theta)\boldsymbol{\mathcal{N}}\cdot\frac{\delta H}{\delta \boldsymbol{v}_h^L} + \theta\boldsymbol{\mathcal{N}}\cdot\frac{\delta H}{\delta \boldsymbol{v}_h^R}, \quad 0 \le \theta \le 1, \end{aligned} \tag{3.14}$$

where we have uniquely defined a left and right side with a positive orientation of the edge numbering per element. Here and hereafter $\boldsymbol{\mathcal{N}} = \boldsymbol{\mathcal{N}}^L$. At edges $e \in \Gamma_b$ at the domain boundary $\partial\Omega_s$, we introduce the boundary conditions (2.3) and (2.11)

$$\widehat{\boldsymbol{\mathcal{N}}\cdot\frac{\delta H}{\delta \boldsymbol{v}_h}} = \boldsymbol{\mathcal{N}} \cdot \mathbf{Q}_h = 0 \quad \text{and} \quad \widehat{\boldsymbol{\mathcal{N}}\cdot\frac{\delta F}{\delta \boldsymbol{v}_h}} = \boldsymbol{\mathcal{N}} \cdot \boldsymbol{\psi} = 0.$$

After the introduction of the numerical fluxes (3.14) and using the fact that each edge occurs twice in the summation over all elements we can rewrite the discrete form of (3.9) as

$$\frac{\mathrm{d}F}{\mathrm{d}t} = \{F, H\}_2 = \sum_{K\in\mathcal{T}_h} \int_K \left(\frac{f_h}{B_h} \frac{\delta F}{\delta \boldsymbol{v}_h}^\perp \cdot \frac{\delta H}{\delta \boldsymbol{v}_h} \right) \mathrm{d}\Omega$$

$$
\begin{aligned}
&+\sum_{K\in\mathcal{T}_h}\int_K\left(\left(\boldsymbol{\mathcal{D}}\cdot\frac{\delta F}{\delta \boldsymbol{v}_h}\right)\frac{\delta H}{\delta \eta_h}+\left(\boldsymbol{\mathcal{D}}\frac{\delta F}{\delta \eta_h}\right)\cdot\frac{\delta H}{\delta \boldsymbol{v}_h}\right)\,\mathrm{d}\Omega\\
&+\sum_{e\in\Gamma_i}\int_e\boldsymbol{\mathcal{N}}\cdot\left(\frac{\delta F}{\delta \boldsymbol{v}_h^R}-\frac{\delta F}{\delta \boldsymbol{v}_h^L}\right)\left(\theta\frac{\delta H}{\delta \eta_h^L}+(1-\theta)\frac{\delta H}{\delta \eta_h^R}\right)\\
&\qquad+\left(\frac{\delta F}{\delta \eta_h^R}-\frac{\delta F}{\delta \eta_h^L}\right)\boldsymbol{\mathcal{N}}\cdot\left(\theta\frac{\delta H}{\delta \boldsymbol{v}_h^R}+(1-\theta)\frac{\delta H}{\delta \boldsymbol{v}_h^L}\right)dS, \qquad (3.15)
\end{aligned}
$$

3.4 The skew-symmetry of the discrete bracket

The discrete bracket (3.15) apparently lacks the skew-symmetry, which would withhold immediate energy conservation. The skew-symmetry of the discrete bracket can, however, be demonstrated using a discretization of the skew-symmetric bracket given by (2.4), and related to the discrete bracket (3.15). This approach will also indicate how to obtain a suitable discretization for bracket $\{\cdot,\cdot\}_1$. The equivalence of these two Hamiltonian discretizations giving (3.10)-(3.11) automatically leads to energy conservation at the discrete level.

The discretization of the bracket $\{\cdot,\cdot\}_1$ in (2.4) yields

$$
\begin{aligned}
\{F,H\}_1=&\sum_{K\in\mathcal{T}_h}\int_K\left(\frac{f_h}{B_h}\frac{\delta F}{\delta \boldsymbol{v}_h}^{\perp}\cdot\frac{\delta H}{\delta \boldsymbol{v}_h}\right)\,\mathrm{d}\Omega\\
&+\sum_{K\in\mathcal{T}_h}\int_K\left(-\frac{\delta F}{\delta \boldsymbol{v}_h}\cdot\left(\boldsymbol{\mathcal{D}}\frac{\delta H}{\delta \eta_h}\right)+\left(\boldsymbol{\mathcal{D}}\frac{\delta F}{\delta \eta_h}\right)\cdot\frac{\delta H}{\delta \boldsymbol{v}_h}\right)\,\mathrm{d}\Omega\\
&+\sum_{K\in\mathcal{T}_h}\int_{\partial K}\left(\widehat{\boldsymbol{\mathcal{N}}\cdot\frac{\delta F}{\delta \boldsymbol{v}_h}}\frac{\delta H}{\delta \eta_h}-\widehat{\boldsymbol{\mathcal{N}}\cdot\frac{\delta H}{\delta \boldsymbol{v}_h}}\frac{\delta F}{\delta \eta_h}\right)dS, \qquad (3.16)
\end{aligned}
$$

where the numerical fluxes $\widehat{\boldsymbol{\mathcal{N}}\cdot\frac{\delta F}{\delta \boldsymbol{v}_h}}$ and $\widehat{\boldsymbol{\mathcal{N}}\cdot\frac{\delta H}{\delta \boldsymbol{v}_h}}$ are introduced. When the numerical flux $\widehat{\boldsymbol{\mathcal{N}}\cdot\frac{\delta F}{\delta \boldsymbol{v}_h}}$ is chosen the same as for $\widehat{\boldsymbol{\mathcal{N}}\cdot\frac{\delta H}{\delta \boldsymbol{v}_h}}$, the discrete bracket is skew-symmetric. Hence energy and mass are then automatically conserved at the discrete level.

For the specific choice of the numerical flux given by (3.14), we obtain for bracket $\{\cdot,\cdot\}_1$ at interior edges $e\in\Gamma_i$

$$
\begin{aligned}
\widehat{\boldsymbol{\mathcal{N}}\cdot\frac{\delta F}{\delta \boldsymbol{v}_h}}=&(1-\theta)\boldsymbol{\mathcal{N}}\cdot\frac{\delta F}{\delta \boldsymbol{v}_h^L}+\theta\boldsymbol{\mathcal{N}}\cdot\frac{\delta F}{\delta \boldsymbol{v}_h^R},\\
\widehat{\boldsymbol{\mathcal{N}}\cdot\frac{\delta H}{\delta \boldsymbol{v}_h}}=&(1-\theta)\boldsymbol{\mathcal{N}}\cdot\frac{\delta H}{\delta \boldsymbol{v}_h^L}+\theta\boldsymbol{\mathcal{N}}\cdot\frac{\delta H}{\delta \boldsymbol{v}_h^R},\quad 0\le\theta\le 1. \qquad (3.17)
\end{aligned}
$$

At the domain boundary $\partial\Omega_s$, we must satisfy for edges $e \in \Gamma_b$, the condition (2.3)

$$\widehat{\boldsymbol{\mathcal{N}}\cdot\frac{\delta H}{\delta \boldsymbol{v}_h}} = \boldsymbol{\mathcal{N}} \cdot \mathbf{Q}_h = 0. \tag{3.18}$$

This implies, in order to ensure the skew symmetry of the bracket, the following boundary condition at $\partial\Omega_s$ on the functional derivative of $\mathcal{F}$

$$\widehat{\boldsymbol{\mathcal{N}}\cdot\frac{\delta F}{\delta \boldsymbol{v}_h}} = \boldsymbol{\mathcal{N}} \cdot \boldsymbol{\psi} = 0. \tag{3.19}$$

Next, we will show now the equivalence of brackets $\{\cdot,\cdot\}_1$ and $\{\cdot,\cdot\}_2$. After integration by parts of (3.16), we obtain

$$\begin{aligned}\{\mathcal{F},\mathcal{H}\}_1 = &\sum_{K\in\mathcal{T}_h}\int_K \left(\frac{f_h}{B_h}\frac{\delta F}{\delta \boldsymbol{v}_h}^{\perp}\cdot\frac{\delta H}{\delta \boldsymbol{v}_h}\right)\mathrm{d}\Omega \\ &+\sum_{K\in\mathcal{T}_h}\int_K \left(\boldsymbol{\mathcal{D}}\cdot\left(\frac{\delta F}{\delta \boldsymbol{v}_h}\right)\frac{\delta H}{\delta \eta_h}+\left(\boldsymbol{\mathcal{D}}\frac{\delta F}{\delta \eta_h}\right)\cdot\frac{\delta H}{\delta \boldsymbol{v}_h}\right)\mathrm{d}\Omega \\ &+\sum_{K\in\mathcal{T}_h}\int_{\partial K}\left(\widehat{\boldsymbol{\mathcal{N}}\cdot\frac{\delta F}{\delta \boldsymbol{v}_h}}\frac{\delta H}{\delta \eta_h}-\widehat{\boldsymbol{\mathcal{N}}\cdot\frac{\delta H}{\delta \boldsymbol{v}_h}}\frac{\delta F}{\delta \eta_h}-\boldsymbol{\mathcal{N}}\cdot\frac{\delta F}{\delta \boldsymbol{v}_h}\frac{\delta H}{\delta \eta_h}\right)dS,\end{aligned} \tag{3.20}$$

where we have used the fact that the functional derivatives of F on an element $K \in \mathcal{T}_h$ are equal to the arbitrary test functions $\boldsymbol{\psi}$ and ϕ, which are zero outside each element K. Therefore it is not necessary to introduce a numerical flux on the last contribution in the integral over the element boundary in (3.20). We introduce now the numerical fluxes (3.17) and boundary conditions (3.18)-(3.19) and use the fact that each interior edge occurs twice in the summation over all elements in the tesssellation. The integral over the element boundaries in (3.20) then can be expressed as

$$\begin{aligned}\sum_{K\in\mathcal{T}_h}\int_{\partial K}&\left(\widehat{\boldsymbol{\mathcal{N}}\cdot\frac{\delta F}{\delta \boldsymbol{v}_h}}\ \frac{\delta H}{\delta \eta_h}-\widehat{\boldsymbol{\mathcal{N}}\cdot\frac{\delta H}{\delta \boldsymbol{v}_h}}\frac{\delta F}{\delta \eta_h}-\boldsymbol{\mathcal{N}}\cdot\frac{\delta F}{\delta \boldsymbol{v}_h}\frac{\delta H}{\delta \eta_h}\right)dS. \\ &=\sum_{e\in\Gamma_i}\int_e\left(\boldsymbol{\mathcal{N}}_L\cdot\left((1-\theta)\frac{\delta F}{\delta \boldsymbol{v}_h^L}+\theta\frac{\delta F}{\delta \boldsymbol{v}_h^R}\right)\left(\frac{\delta H}{\delta \eta_h^L}-\frac{\delta H}{\delta \eta_h^R}\right)\right. \\ &\qquad+\boldsymbol{\mathcal{N}}_L\cdot\left((1-\theta)\frac{\delta H}{\delta \boldsymbol{v}_h^L}+\theta\frac{\delta H}{\delta \boldsymbol{v}_h^R}\right)\left(\frac{\delta F}{\delta \eta_h^R}-\frac{\delta F}{\delta \eta_h^L}\right) \\ &\qquad\left.+\boldsymbol{\mathcal{N}}_L\cdot\frac{\delta F}{\delta \boldsymbol{v}_h^R}\frac{\delta H}{\delta \eta_h^R}-\boldsymbol{\mathcal{N}}_L\cdot\frac{\delta F}{\delta \boldsymbol{v}_h^L}\frac{\delta H}{\delta \eta_h^L}\right)dS,\end{aligned}$$

which can be simplified into

$$\sum_{K\in\mathcal{T}_h}\int_{\partial K}\left(\widehat{\boldsymbol{\mathcal{N}}\cdot\frac{\delta F}{\delta \boldsymbol{v}_h}}\ \frac{\delta H}{\delta \eta_h}-\widehat{\boldsymbol{\mathcal{N}}\cdot\frac{\delta H}{\delta \boldsymbol{v}_h}}\frac{\delta F}{\delta \eta_h}-\boldsymbol{\mathcal{N}}\cdot\frac{\delta F}{\delta \boldsymbol{v}_h}\frac{\delta H}{\delta \eta_h}\right)dS.$$
$$=\sum_{e\in\Gamma_i}\int_e\left(\boldsymbol{\mathcal{N}}_L\cdot\left(\frac{\delta F}{\delta \boldsymbol{v}_h^R}-\frac{\delta F}{\delta \boldsymbol{v}_h^L}\right)\left(\theta\frac{\delta H}{\delta \eta_h^L}+(1-\theta)\frac{\delta H}{\delta \eta_h^R}\right)\right. \tag{3.21}$$
$$\left.+\boldsymbol{\mathcal{N}}_L\cdot\left((1-\theta)\frac{\delta H}{\delta \boldsymbol{v}_h^L}+\theta\frac{\delta H}{\delta \boldsymbol{v}_h^R}\right)\left(\frac{\delta F}{\delta \eta_h^R}-\frac{\delta F}{\delta \eta_h^L}\right)\right)dS.$$

Combining (3.20) and (3.21) the final result equals (3.15) and proves that the bracket $\{\cdot,\cdot\}_2$ is also skew-symmetric.

The skew-symmetry of the discrete bracket immediately implies the following properties:

Proposition 3.1. *(energy and mass conservation) The solution to the Hamiltonian formulation (3.10) - (3.11) satisfies energy and mass conservation at the discrete level, i.e.*

$$\frac{\mathrm{d}}{\mathrm{d}t}H=0\quad \textit{and}\quad \frac{\mathrm{d}}{\mathrm{d}t}M=0,$$

where

$$H=\frac{1}{2}\sum_K\int_K\left(B_h\left|\boldsymbol{v}_h\right|^2+C_h\,\eta_h^2\right)\,\mathrm{d}\Omega\quad \textit{and}\quad M=\sum_K\int_K\eta_h\,\mathrm{d}\Omega.$$

3.5 DG scheme

In this section, we compare the discontinuous Hamiltonian formulation with a DG formulation. Multiplying (2.2) with arbitrary test functions $\boldsymbol{\psi}\in V_h\times V_h$ and $\phi\in V_h$, and integrating by parts over each element $K\in\mathcal{T}_h$, we obtain the following relation for $\boldsymbol{v}_h\in V_h\times V_h$ and $\eta_h\in V_h$:

$$\int_K\frac{\partial \boldsymbol{v}_h}{\partial t}\cdot\boldsymbol{\psi}\mathrm{d}\Omega=\int_K(-f\boldsymbol{v}_h^{\perp}\cdot\boldsymbol{\psi}+C\eta_h\boldsymbol{\mathcal{D}}\cdot\boldsymbol{\psi})\mathrm{d}\Omega-\int_{\partial K}\widehat{C\eta_h}\boldsymbol{\mathcal{N}}\cdot\boldsymbol{\psi}\mathrm{d}s, \tag{3.22}$$
$$\int_K\frac{\partial \eta_h}{\partial t}\phi\mathrm{d}x\mathrm{d}y=\int_K(B_h\boldsymbol{v}_h)\cdot\boldsymbol{\mathcal{D}}\phi\mathrm{d}\Omega-\int_{\partial K}\boldsymbol{\mathcal{N}}\cdot\widehat{(B_h\boldsymbol{v}_h)}\phi\mathrm{d}S, \tag{3.23}$$

where we choose, motivated by the numerical fluxes used for the Hamiltonian formulation, discussed in Sections 3.3-3.4, and stability reasons ([14]), the following alternating numerical fluxes

$$\widehat{C\eta_h}=\theta C\eta_h^L+(1-\theta)C\eta_h^R, \tag{3.24}$$

$$\widehat{\boldsymbol{\mathcal{N}}\cdot(B_h\boldsymbol{v}_h)} = (1-\theta)\boldsymbol{\mathcal{N}}\cdot(B_h\boldsymbol{v}_h)^L + \theta\boldsymbol{\mathcal{N}}\cdot(B_h\boldsymbol{v}_h)^R, \quad 0 \le \theta \le 1.$$

At edges at the domain boundary we impose the physical boundary condition (2.3), which states

$$\boldsymbol{\mathcal{N}}\cdot\boldsymbol{v}_h = 0.$$

The DG scheme (3.22)–(3.23) for constant B_h and C_h equals the Hamiltonian discontinuous finite element scheme and then also satisfies energy conservation. These restrictions imply that $B_h\boldsymbol{v}_h$ and $C_h\,\eta_h$ belong to the Galerkin test function space. For general nonconstant B_h and C_h, energy conservation can not be obtained from the classical DG method (3.22)-(3.23). In the linear case, however, we can weight the usual test function with B_h to alleviate this problem.

4 Time discretization

We compare two time discretization methods. First, the non-symplectic and dissipative third-order total variation diminishing Runge-Kutta method of [13] is used. Next, we consider a symplectic splitting method for Hamiltonian systems [6].

4.1 Third order TVD Runge-Kutta

An explicit third order Runge-Kutta method [13] for solving

$$\dot{u} = L(u,t), \tag{4.1}$$

where $L(u,t)$ is a spatial discretization operator, is defined as

$$\begin{aligned} u^{(1)} &= u^n + \Delta t L(u^n, t^n), \\ u^{(2)} &= \frac{3}{4}u^n + \frac{1}{4}u^{(1)} + \frac{1}{4}\Delta t L(u^{(1)}, t^n + \Delta t), \\ u^{n+1} &= \frac{1}{3}u^n + \frac{2}{3}u^{(2)} + \frac{2}{3}\Delta t L(u^{(2)}, t^n + \frac{1}{2}\Delta t). \end{aligned} \tag{4.2}$$

4.2 Symplectic splitting method

The TVD Runge-Kutta method discussed in Section 4.1 is slightly dissipative. In order to ensure energy conservation we consider therefore a symplectic time integration method. The following ordinary differential equations arise from the Hamiltonian spatial discretization, for each element

$$\begin{aligned} M_{ij}\,\frac{\mathrm{d}\hat{\boldsymbol{v}}_j}{\mathrm{d}t} &= -\,O_{ij}\,\hat{\mathbf{Q}}_j + \mathbf{G}_{ij}\,\hat{r}_j - \int_{\partial K} \boldsymbol{\mathcal{N}}\,\hat{r}_h\,\psi_i\,\mathrm{d}s \\ M_{ij}\,\frac{\mathrm{d}\hat{\eta}_j}{\mathrm{d}t} &= \mathbf{G}_{ij}\boldsymbol{\cdot}\hat{\mathbf{Q}}_j - \int_{\partial K} \widehat{\boldsymbol{\mathcal{N}}\boldsymbol{\cdot}\mathbf{Q}_h}\,\psi_i\,\mathrm{d}s \\ M_{ij}\,\hat{\mathbf{Q}}_j &= B_{ij}\,\hat{\boldsymbol{v}}_j \quad \text{and} \quad M_{ij}\,\hat{r}_j = C_{ij}\,\hat{\eta}_j \end{aligned} \tag{4.3}$$

with elemental coefficients $\hat{r}_j$ and $\hat{\boldsymbol{v}}_j$, basis functions ψ_i or ψ_j, and elemental matrices

$$\begin{aligned} M_{ij} &= \int_K \psi_i\,\psi_j\,\mathrm{d}x\,\mathrm{d}y \\ B_{ij} &= \int_K B_h\,\psi_i\,\psi_j\,\mathrm{d}x\,\mathrm{d}y \\ C_{ij} &= \int_K C_h\,\psi_i\,\psi_j\,\mathrm{d}x\,\mathrm{d}y \\ \mathbf{G}_{ij} &= \int_K \psi_j\,\boldsymbol{\mathcal{D}}\,\psi_i\,\mathrm{d}x\,\mathrm{d}y \\ O_{ij} &= \int_K \frac{f_h}{B_h}\,\psi_i\,\psi_j\,\mathrm{d}x\,\mathrm{d}y. \end{aligned} \tag{4.4}$$

We write the Hamiltonian spatial discretization (4.3)–(4.4) abstractly in the form

$$\frac{\mathrm{d}\hat{\boldsymbol{v}}_K}{\mathrm{d}t} = L_1\,\hat{\boldsymbol{v}}_K + L_2\,\hat{\eta}, \quad \frac{\mathrm{d}\hat{\eta}_K}{\mathrm{d}t} = L_3\,\hat{\boldsymbol{v}}, \tag{4.5}$$

where $\hat{\boldsymbol{v}}$ and $\hat{\eta}$ are the expansion coefficients, specifically denoted in element K by $\hat{\boldsymbol{v}}_K$ and $\hat{\eta}_K$, and L_1, L_2, L_3 are the appropriate constant matrices independent of the variables. The matrix L_1 only involves local integrals per element and no face integrals, as follows from (4.3). In contrast, L_2 and L_3 depend on face integrals as well. Note that, for conciseness of presentation, we explicitly eliminated $\mathbf{Q}_h$ and r_h.

The linear system (4.5) is a generalized Poisson system with a quadratic Hamiltonian depending on a quadratic term with velocity coefficients $\hat{\boldsymbol{v}}$ plus one with coefficients $\hat{\eta}$. A second order symplectic partitioned Runge-Kutta time integration method is now based on this splitting of the Hamiltonian $H = H_v + H_\eta$ in two separate quadratic parts. The resulting time discretization consists of the composition of exactly integrable pieces, one half step of the Hamiltonian

dynamics using only the Hamiltonian H_v, a complete time step using the Hamiltonian H_η and than one half time step using only the Hamiltonian H_v again. We therefore employ exactly integrable linear Poisson systems in turn, as suggested in [6]. For $f = 0$ we then basically obtain the Störmer-Verlet method for our linear system [6]. For nonzero and constant f, and constant function B, the velocity $\hat{\boldsymbol{v}}$ in the first and last split time step can be solved exactly. For nonzero and nonconstant f and B, the solution for $\hat{\boldsymbol{v}}$ in a split time step is local and harmonic, but its coefficients require a numerical determination. The resulting symplectic method does require a constant time step. The linear dispersion relations yield approximate time step requirements.

With $\tau = \Delta t$, and the case with f and B constant, the resulting numerical scheme for (4.5) becomes

$$\tilde{\mathbf{U}}_{int} = \frac{1}{f} \begin{pmatrix} \sin(f\tau/2) & (1-\cos(f\tau/2)) \\ (\cos(f\tau/2)-1) & \sin(f\tau/2) \end{pmatrix} \begin{pmatrix} \hat{u}^n \\ \hat{v}^n \end{pmatrix} \tag{4.6a}$$

$$\hat{\eta}^{n+1/2} = \hat{\eta}^n + L_3\, \tilde{\mathbf{U}}_{int} \tag{4.6b}$$

$$\forall K: \quad \begin{pmatrix} \hat{u}_j^{n+1/2} \\ \hat{v}_j^{n+1/2} \end{pmatrix} = \begin{pmatrix} \cos(f\tau/2) & \sin(f\tau/2) \\ -\sin(f\tau/2) & \cos(f\tau/2) \end{pmatrix} \begin{pmatrix} \hat{u}^n \\ \hat{v}^n \end{pmatrix} \tag{4.6c}$$

$$\tilde{\boldsymbol{v}}^{n+1} = \hat{\boldsymbol{v}}^{n+1/2} - \tau\, L_2\, \hat{\eta}^{n+1/2} \tag{4.6d}$$

$$\forall K: \quad \begin{pmatrix} \hat{u}_j^{n+1} \\ \hat{v}_j^{n+1} \end{pmatrix} = \begin{pmatrix} \cos(f\tau/2) & \sin(f\tau/2) \\ -\sin(f\tau/2) & \cos(f\tau/2) \end{pmatrix} \begin{pmatrix} \tilde{u}^{n+1} \\ \tilde{v}^{n+1} \end{pmatrix} \tag{4.6e}$$

$$\mathbf{U}_{int}^{n+1} = \frac{1}{f} \begin{pmatrix} \sin(f\tau/2) & (1-\cos(f\tau/2)) \\ (\cos(f\tau/2)-1) & \sin(f\tau/2) \end{pmatrix} \begin{pmatrix} \hat{u}^{n+1} \\ \hat{v}^{n+1} \end{pmatrix} \tag{4.6f}$$

$$\hat{\eta}^{n+1} = \hat{\eta}^{n+1/2} + L_3\, \mathbf{U}_{int}^{n+1}. \tag{4.6g}$$

In (4.6a) with both f and B constant, we have obtained $\mathbf{U}_{int}$ by integrating the following ordinary differential equations for the local coefficients $\hat{\boldsymbol{v}}_j$ per element exactly:

$$\frac{\mathrm{d}\hat{\boldsymbol{v}}_j}{\mathrm{d}t} = -\, f\, \hat{\boldsymbol{v}}_j^{\perp}. \tag{4.7}$$

For nonconstant f and B, the splitting scheme in time becomes slightly more involved.

5 Numerical results

In this section, we provide numerical examples to illustrate the accuracy and capability of the methods developed in the previous section. In all examples, the figures present the solution obtained with a particular choice of the mesh. We have verified with the aid of successive mesh refinements, that in all cases, the results shown are numerically convergent.

5.1 Rotating linear shallow water equations

In the first set of test cases we consider wave problems governed by the rotating linear shallow water equations on an f-plane, given by (2.12). The tests involve harmonic waves, Kelvin and Poincaré waves, and linear waves in a closed parabolic bowl.

5.1.1 Harmonic waves

Consider a two-dimensional (2D) harmonic wave solution of (2.12) for a constant topography $D = H$ and constant f in a periodic domain $L_x \times L_y$. Exact solutions of this problem are given in Appendix A. First, we consider the accuracy for the parameters given in (A.2). The L^2 and L^∞ errors and the numerical orders of accuracy for the water depth η are given in Table 5.1 at time $t = 1$ on a uniform rectangular mesh in the domain $[0, 1] \times [0, 1]$. We see that the method with P^k elements gives a uniform (k+1)-th order of accuracy in both norms.

We also present the wave profile using P^1 elements on a uniform rectangular 80×80 mesh at $t = 100$ for the parameters given in (A.3). In Figure 5.1, the water depth η is shown at time $t = 100$ as well as the energy as function of time. The discontinuous Hamiltonian and DG formulation coincide in this case, and we therefore compare the Runge-Kutta and symplectic splitting time discretizations. The results show that the symplectic time integration scheme is better in energy conservation than a third order TVD Runge-Kutta method.

Table 5.1: Accuracy test for the water depth η of the linear shallow water equations (2.12) with exact solution (A.1). Periodic boundary conditions. Uniform meshes containing $N_x \times N_y$ cells at time $t = 1$.

	$N_x \times N_y$	L^2 error	order	L^∞ error	order
P^0	20×20	3.70E-01	–	1.13E-00	–
	40×40	1.48E-01	1.32	4.54E-01	1.31
	80×80	8.89E-02	0.74	2.87E-01	0.66
	160×160	5.01E-02	0.83	1.58E-01	0.86
P^1	20×20	8.86E-02	–	3.94E-01	–
	40×40	1.75E-02	2.34	9.36E-02	2.07
	80×80	5.11E-03	1.78	2.28E-02	2.04
	160×160	1.10E-03	2.22	5.17E-03	2.14
P^2	20×20	2.09E-02	–	9.61E-02	–
	40×40	1.67E-03	3.64	7.49E-03	3.68
	80×80	1.95E-04	3.09	1.38E-03	2.44
	160×160	1.93E-05	3.34	7.61E-05	4.18
P^3	20×20	1.84E-03	–	1.17E-02	–
	40×40	1.22E-04	3.92	6.06E-04	4.27
	80×80	6.68E-06	4.19	4.10E-05	3.88
	160×160	3.85E-07	4.11	2.26E-06	4.18

5.1.2 Kelvin and Poincaré waves

We consider Kelvin and Poincaré waves for the shallow water equations (2.12). These are specific normal-mode solutions of the rotating shallow water equations. Kelvin waves arise as boundary-trapped modes in the precense of rotation; on the Northern hemisphere where $f > 0$ these modes propagate counterclockwise with the boundary on the right. Poincaré modes are gravity modes modified by the Earth's rotation. These eigenmodes in turn test the numerical scheme in the

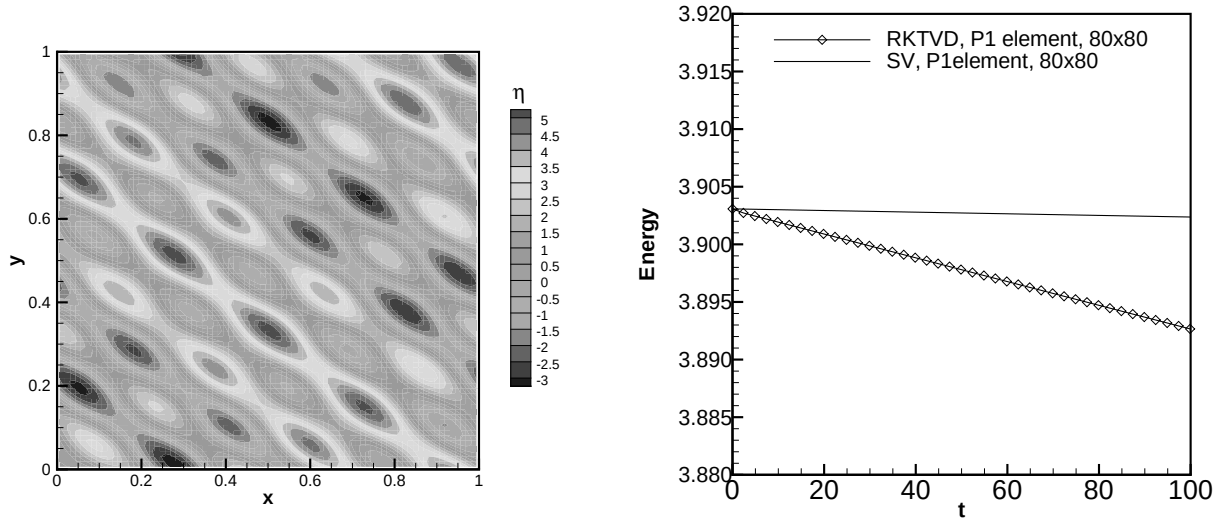

Figure 5.1: Harmonic waves described by the linear rotating shallow water equations (2.12) at $t = 100$ and the discrete energy for the symplectic splitting (SV) and TVD Runge-Kutta (RKTVD) time integration methods.

precense of boundaries and rotation.

The exact solutions for three different cases are given in Appendices B.1, B.2 and B.3. In Figures 5.2 and 5.3, we show respectively Kelvin waves and Poincaré waves at $t = 100$ in a rectangular channel periodic in x using P^1 elements on an unstructured triangular mesh (1000 elements). We also plot the discrete energy using the TVD Runge-Kutta (TVDRK) and the symplectic splitting (SV) time integration methods. In Fig. 5.4, we show the Poincaré waves in a circular basin using P^1 elements on an unstructured triangular mesh (1000 elements) after 100 periods and the discrete energy for the symplectic splitting time integration schemes. The TVD Runge-Kutta method, however, did not survive a long time simulation for the Poincaré waves and will blowup after a few wave periods. We only give therefore the energy results for the symplectic scheme.

The Hamiltonian and the DG finite element scheme coincide in these test cases because the bottom topography is constant. The energy in all these examples is conserved very well with the discontinuous Hamiltonian discretization in combination with the splitting time integration method, even for unstructured meshes and with solid wall boundary conditions. The results show

that the symplectic scheme is more accurate in conserving energy and also more stable than a third order TVD Runge-Kutta method.

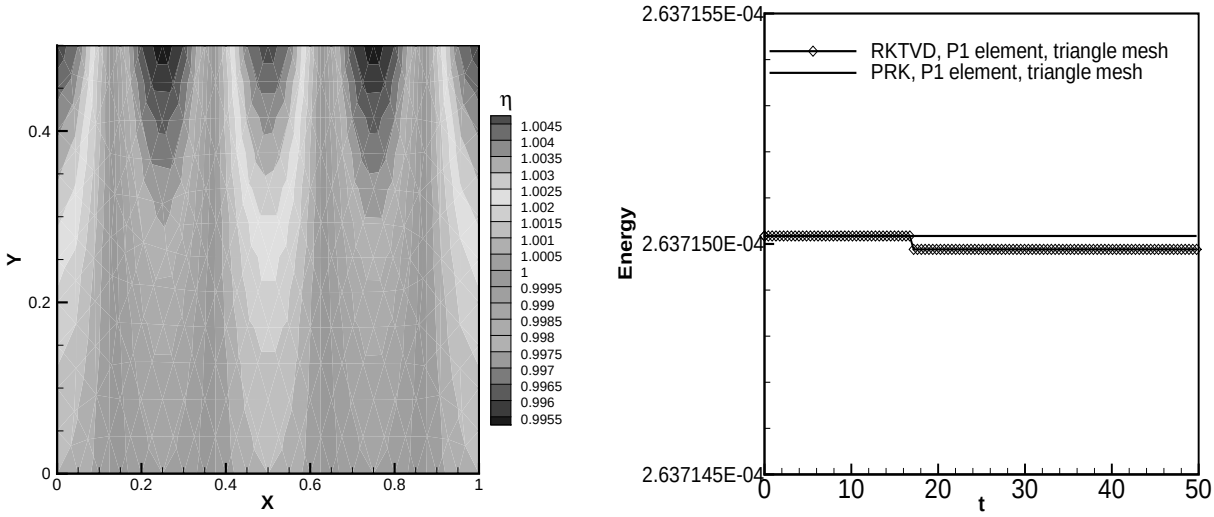

Figure 5.2: Kelvin waves described by the linear rotating shallow water equations (2.12) in a rectangular domain after 100 periods and the discrete energy for the TVD Runge-Kutta (TVDRK) and the symplectic splitting (PRK) time integration methods.

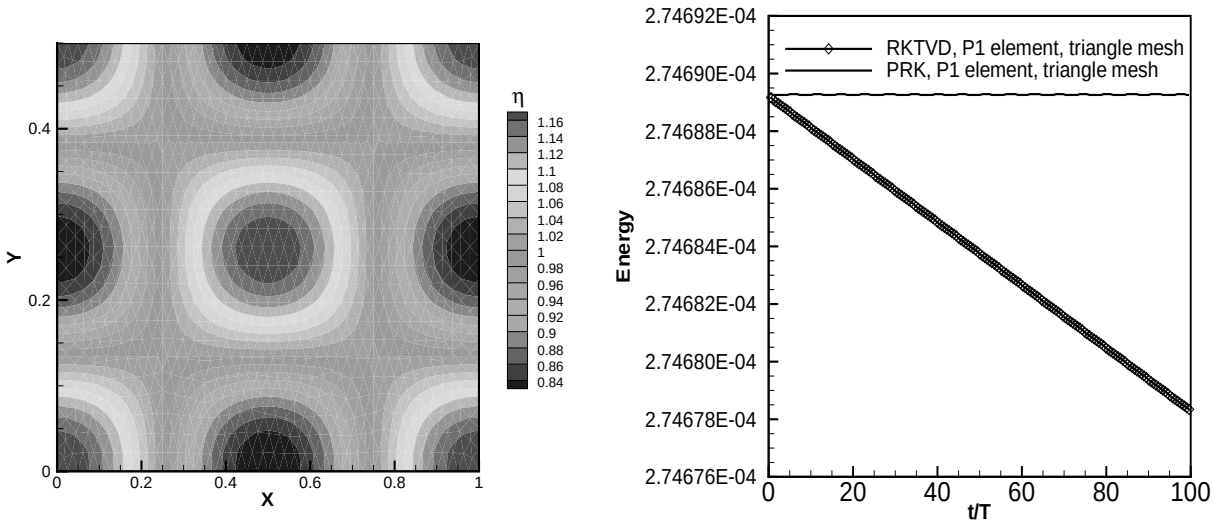

Figure 5.3: Poincaré waves described by the linear rotating shallow water equations (2.12) in a rectangular domain after 100 periods and the discrete energy for the TVD Runge-Kutta (TVDRK) and the symplectic splitting (PRK) time integration methods.

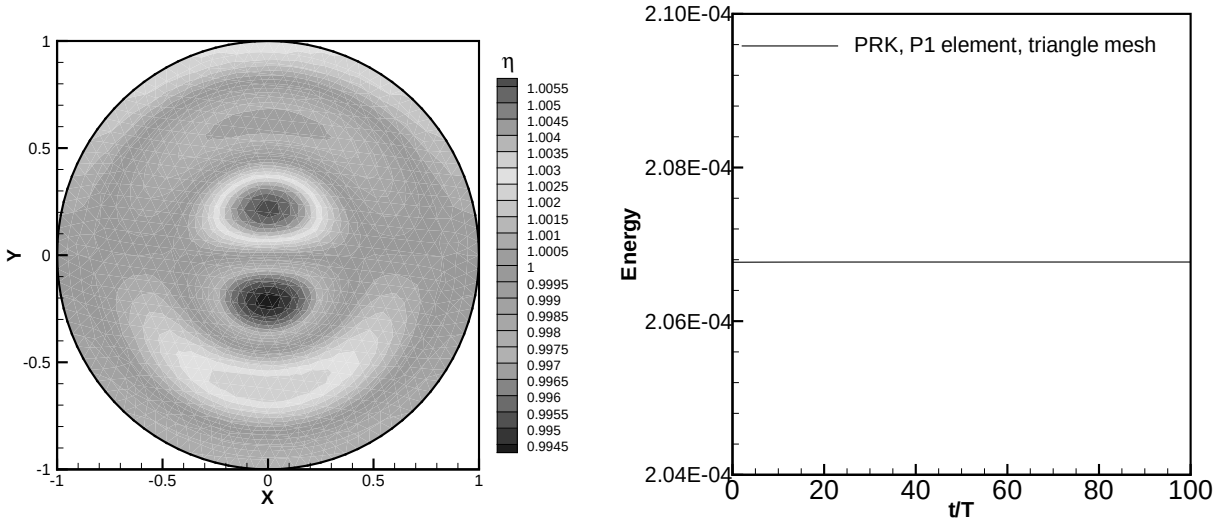

Figure 5.4: Poincaré waves described by the linear rotating shallow water equations (2.12) in a circular domain after 100 periods and the discrete energy for the symplectic splitting (PRK) time integration methods. The TVDRK method is unstable for this case.

5.1.3 Linear waves in closed parabolic bowl

To test the Hamiltonian discretization against the classical non-Hamiltonian DG scheme, we consider linear non-rotating shallow water equations (2.12) with $f = 0$ in a closed circular parabolic bowl. Hence, the topography is varying: $D = D(x, y) = D_0\ (1 - (x^2 + y^2)/a^2)$ and the DG scheme is not energy preserving anymore. One of the exact solutions of equation (2.12) is given in Appendix C. In Fig. 5.5, we show the waves by the Hamiltonian formulation and the DG scheme in a circular basin for P^1 elements with unstructured triangular meshes (1000 elements) for equations (2.12) after 100 periods and energy conservation. The results show that the discontinuous Hamiltonian discretization and the DG scheme can both approximately preserve the discrete energy.

5.2 Two-dimensional Maxwell equations

Consider the two-dimensional Maxwell equations

$$\frac{\partial \boldsymbol{H}}{\partial t} = \boldsymbol{\nabla}^{\perp} E_z, \quad \frac{\partial E_z}{\partial t} = \boldsymbol{\nabla}^{\perp} \boldsymbol{H}, \tag{5.1}$$

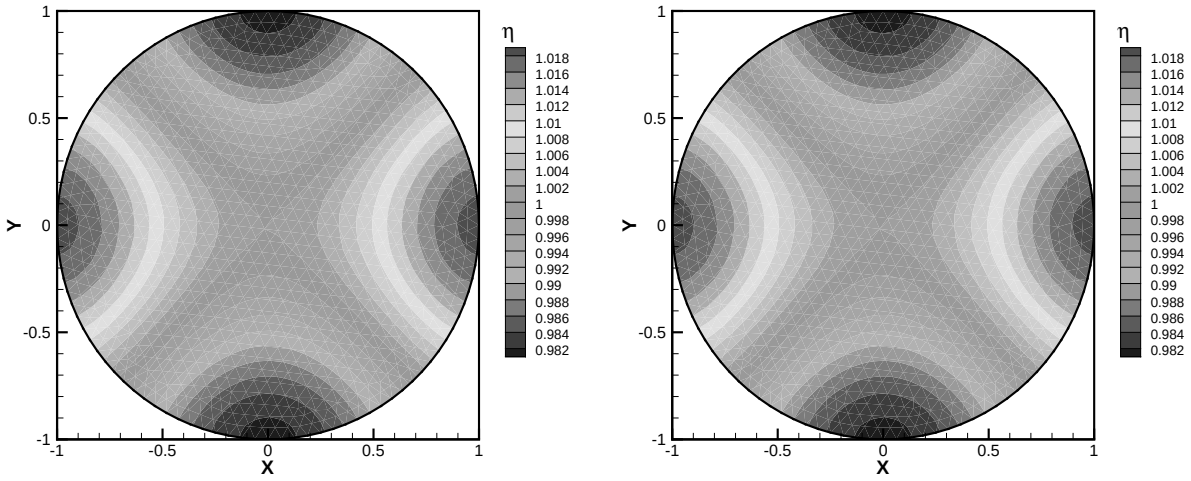

Figure 5.5: Coastal shelf waves for equation described by the linear rotating shallow water equations (2.12) after 100 periods. Left: Hamiltonian discretization. Right: DG scheme.

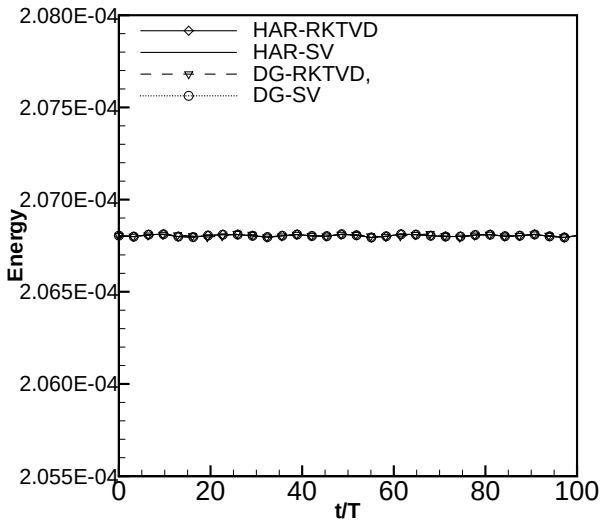

Figure 5.6: The energy is shown for an eigenmode in a circular basin over 100 periods for the Hamiltonian and DG spatial discretizations, and both Runge-Kutta and Störmer-Verlet time discretizations.

with uniform dielectric permittivity and magnetic permeability. The computational domain is $[0, 2\pi/\alpha] \times [0, 2\pi/\beta]$ with periodic boundary conditions. The final simulation time is $t = 100$ (100 periods). The smooth and non-smooth exact solutions of equation (5.1) used in this test case are given in Appendix D.

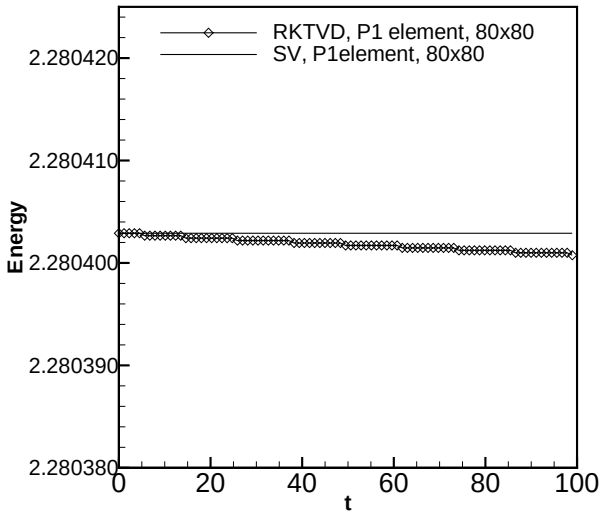

Figure 5.7: Energy for smooth solution (D.1) of the Maxwell equations (5.1).

For the smooth solution, the L^2 and L^∞ errors and the numerical orders of accuracy for H_x, H_y and E_z on a uniform rectangular mesh using periodic boundary conditions are presented in Tables 5.2, 5.3 and 5.4. For this constant coefficient case the Hamiltonian and DG scheme are identical.

We can see that the discretization using P^k elements gives a uniform $(k+1)$-th order of accuracy in both norms. We also show the discrete energy in Fig. 5.7 using P^1 elements on a uniform rectangular 80×80 mesh. The results show that the symplectic scheme is better than a third order TVD Runge-Kutta method in energy conservation.

For the non-smooth solution we show the numerical results using P^1 elements on a uniform rectangular 80×80 mesh for H_x, H_y and E_z of solution (D.2a) at $t = 100$ in Fig. 5.8. The energy shown in Fig. 5.9 is also conserved very well for the solution with a singularity for the symplectic time integration scheme, whereas the third order TVD Runge-Kutta method is dissipative.

6 Conclusion

In this article we have developed a discontinuous finite element discretization for bilinear Poisson brackets, which can conserve energy and mass because it preserves the skew-symmetry of the

Table 5.2: Errors in the x-component of the magnetic field H_x for smooth solution (D.1) of the Maxwell equations (5.1) at $t = 100$.

	$N_x \times N_y$	L^2 error	order	L^∞ error	order
P^0	20×20	4.29E-01	–	1.02E-00	–
	40×40	1.81E-01	1.24	5.24E-01	0.96
	80×80	5.88E-02	1.62	1.94E-01	1.43
	160×160	2.09E-02	1.49	8.17E-02	1.25
P^1	20×20	3.74E-02	–	1.92E-01	–
	40×40	4.64E-03	3.01	3.96E-02	2.28
	80×80	9.98E-04	2.22	9.20E-03	2.10
	160×160	2.47E-04	2.01	2.28E-03	2.02
P^2	20×20	2.09E-03	–	1.75E-02	–
	40×40	2.26E-04	3.21	2.22E-03	2.98
	80×80	2.82E-05	3.00	3.01E-04	2.88
	160×160	3.47E-06	3.02	3.60E-05	3.06

Poisson bracket at the discrete level. For comparison, we also have presented a classical DG method. Numerical examples illustrate the accuracy and capability of the methods. These examples show that the discontinuous Hamiltonian finite element discretization developed in this article in combination with a symplectic splitting method for the time integration preserves the discrete energy even on unstructured meshes. This makes the discontinuous Hamiltonian discretization an excellent numerical scheme for long time integration of physical problems described by a bilinear Poisson bracket.

In contrast, the discontinuous Galerkin discretization only preserves the discrete energy in the constant coefficient case, but not in general. As an alternative time integration method, we also considered the simpler, third order accurate TVD Runge-Kutta time integration. This time integration method results, however, in most test cases in a decrease of the discrete energy.

Table 5.3: Errors in the y-component of the magnetic field H_y for smooth solution (D.1) of the Maxwell equations (5.1) at $t = 100$.

	$N_x \times N_y$	L^2 error	order	L^∞ error	order
P^0	20×20	3.12E-01	–	7.42E-01	–
	40×40	1.32E-01	1.24	3.81E-01	0.96
	80×80	4.28E-02	1.62	1.41E-01	1.43
	160×160	1.52E-02	1.49	5.93E-02	1.25
P^1	20×20	2.78E-02	–	1.45E-01	–
	40×40	3.41E-03	3.03	2.93E-02	2.30
	80×80	7.27E-04	2.23	6.72E-03	2.13
	160×160	1.80E-04	2.01	1.66E-03	2.02
P^2	20×20	1.56E-03	–	1.43E-02	–
	40×40	1.70E-04	3.45	2.50E-03	3.12
	80×80	2.08E-05	3.03	2.29E-04	2.83
	160×160	2.60E-06	3.00	2.77E-05	3.04

Although not addressed in this article, the methodology is expected to apply to other cases as the generalized linear system of Huttunen et al. [7] and the three-dimensional acoustic equations [2]. We plan to explore this subject in our future research.

Acknowledgments

O.B. was supported by a fellowship of the The Netherlands Academy of Arts and Sciences during part of this research. We thank Albert Wildeman, Bob Peeters and Sid Visser for valuable discussions on the symplectic time splitting method.

Table 5.4: Errors in the z-component of the electric field E_z for smooth solution (D.1) of the Maxwell equations (5.1) at $t = 100$.

	$N_x \times N_y$	L^2 error	order	L^∞ error	order
P^0	20×20	4.76E-01	–	1.25E-00	–
	40×40	1.64E-01	1.53	5.75E-01	1.12
	80×80	4.82E-02	1.77	2.09E-01	1.46
	160×160	1.77E-02	1.44	7.53E-02	1.47
P^1	20×20	4.26E-02	–	1.57E-01	–
	40×40	5.18E-03	3.04	4.31E-02	1.86
	80×80	1.14E-03	2.18	1.11E-02	1.95
	160×160	2.82E-04	2.02	2.80E-03	2.00
P^2	20×20	2.10E-03	–	2.18E-02	–
	40×40	1.92E-04	3.45	2.50E-03	3.12
	80×80	2.37E-05	3.02	3.09E-04	3.02
	160×160	2.99E-06	3.00	4.11E-05	2.91

A The exact solution of equations (2.12)

The exact solution of equations (2.12) with periodic boundary conditions on a domain $L_x \times L_y$ is:

$$\begin{aligned}
\eta &= \sum_{s=\pm 1} \sum_{m,n=-\infty}^{\infty} \left(A_{mns} \cos(z) + B_{mns} \sin(z)\right), \\
u &= \sum_{s=\pm 1} \sum_{m,n=-\infty}^{\infty} \left(C_{mns} \cos(z) + D_{mns} \sin(z)\right), \\
v &= \sum_{s=\pm 1} \sum_{m,n=-\infty}^{\infty} \left(E_{mns} \cos(z) + F_{mns} \sin(z)\right), \\
z &= k_m\, x + l_n\, y + \omega_{mns}\, t,
\end{aligned} \tag{A.1}$$

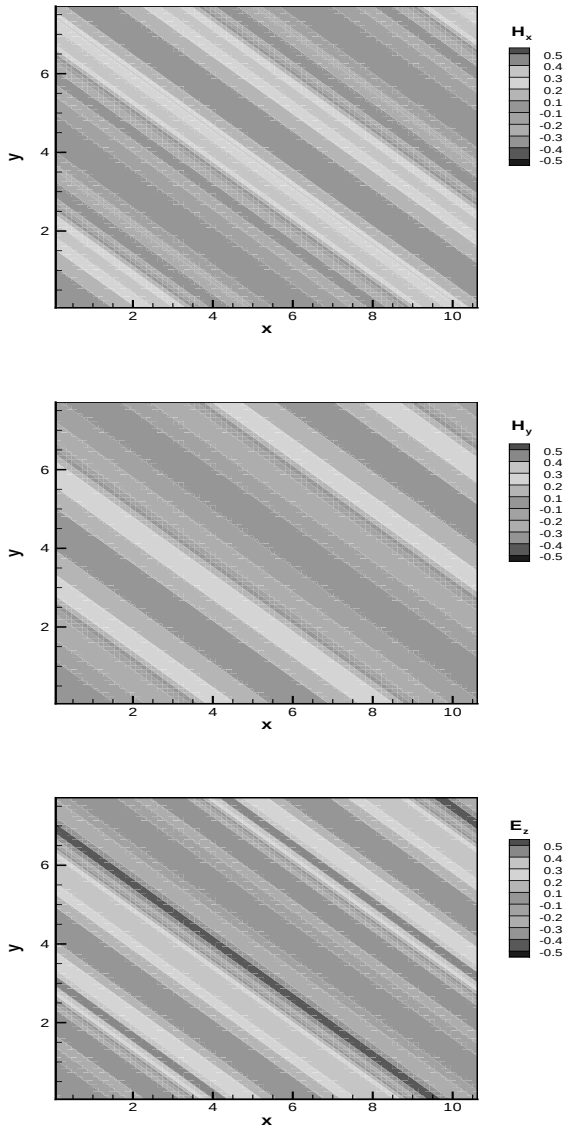

Figure 5.8: The contour plots for H_x, H_y and E_z of solution (D.2a) at $t = 100$.

where

$$C_{mns} = g\,\frac{k_m\,\omega_{mns}\,A_{mns} - f\,l_n\,B_{mns}}{f^2 - \omega_{mns}^2},$$
$$D_{mns} = g\,\frac{k_m\,\omega_{mns}\,B_{mns} + f\,l_n\,A_{mns}}{f^2 - \omega_{mns}^2},$$
$$E_{mns} = g\,\frac{l_n\,\omega_{mns}\,A_{mns} + f\,k_m\,B_{mns}}{f^2 - \omega_{mns}^2},$$
$$F_{mns} = g\,\frac{l_m\,\omega_{mns}\,B_{mns} - f\,k_m\,A_{mns}}{f^2 - \omega_{mns}^2},$$
$$k_m = \frac{2\,\pi\,m}{L_x}, \quad l_n = \frac{2\,\pi\,n}{L_y},$$

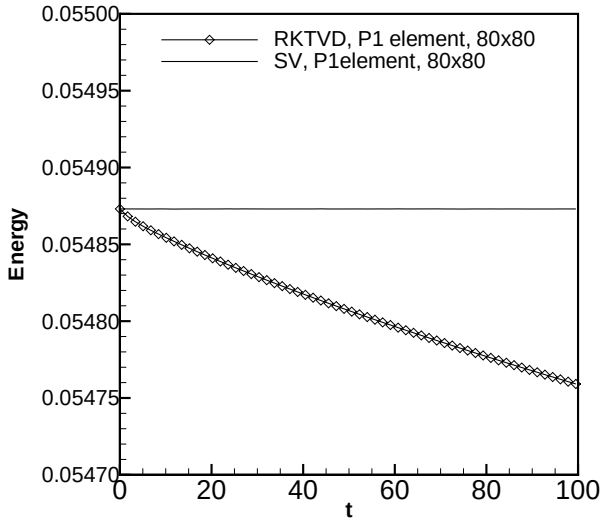

Figure 5.9: Energy for non-smooth solution (D.2a) of the Maxwell equations (5.1).

$$\omega_{mn\pm} = \pm\sqrt{(f^2 + g\,H\,(k_m^2 + l_n^2))}$$

with m, n are integers. The coefficients A_{mns} and B_{mns} are arbitrary amplitudes with indices m, n, s and L_x and L_y the lengths of the domain in the x and y directions, respectively. We use the following two sets of parameters

$$\begin{aligned} &f = 1,\ g = 1,\ H = 1, \\ &k_1 = 1,\ l_1 = 1,\ s_1 = 1,\ A_1 = 1,\ B_1 = 1 \\ &k_2 = 2,\ l_2 = -3,\ s_2 = -1,\ A_2 = 0.8,\ B_2 = 0.6. \end{aligned} \tag{A.2}$$

and

$$\begin{aligned} &f = 1,\ g = 1,\ H = 1, \\ &k_1 = 1,\ l_1 = 1,\ s_1 = 1,\ A_1 = 1,\ B_1 = 1 \\ &k_2 = 2,\ l_2 = -3,\ s_2 = -1,\ A_2 = 0.8,\ B_2 = 0.6, \\ &k_3 = 4,\ l_3 = 5,\ s_3 = 1,\ A_3 = 1.2,\ B_3 = 1.5. \end{aligned} \tag{A.3}$$

B Kelvin and Poincaré waves

B.1 Kelvin wave in a rectangular domain

A Kelvin wave in a rectangular domain $[0, L_x] \times [0, L_y]$ is given by

$$u(x, y, t) = \frac{(\omega k - fl)gA}{f^2 - \omega^2} e^{ly} \cos(kx + \omega t), \tag{B.1}$$

$$v(x, y, t) = 0,$$

$$\eta(x, y, t) = H + Ae^{ly} \cos(kx + \omega t), \tag{B.2}$$

with $a^2 = gH$, periodic boundary conditions in the x direction and solid wall boundary conditions in the y direction. H is the mean free surface height, $\omega = ak$ is the dispersion relation, $l = f/a$, $k = 2\pi m/L_x$ are the wave numbers and m is an arbitrary integer. The parameters are the following: $A = 0.001,\ H = 1.0,\ L_x = 1.0\ , L_y = 0.5,\ m = 2,\ g = 1,\ f = 3.193379349.$

B.2 Poincaré wave in a rectangular domain

A Poincaré wave in a rectangular domain $[0, L_x] \times [0, L_y]$ is given by

$$\begin{aligned} u(x, y, t) &= \frac{gA}{f^2 - \omega^2}(-kl(f^2 - \omega^2)\cos(ly) + fk\sin(ly))\cos(kx + \omega t), \\ v(x, y, t) &= -\frac{gA}{f^2 - \omega^2}((fk)^2 + (\omega l)^2)\sin(ly)\sin(kx + \omega t), \\ \eta(x, y, t) &= H + A(\omega l \cos(ly) + fk\sin(ly))\cos(kx + \omega t), \end{aligned} \tag{B.3}$$

with $a^2 = gH$, periodic boundary conditions in x and solid wall boundary conditions in y. $\omega^2 = f^2 + a^2(k^2 + l^2)$ is the dispersion relation, $k = 2\pi m/L_x$, $l = 2\pi n/L_y$ are the wave numbers and m, n are any integers. The parameters are the following: $A = 1.0E - 05,\ H = 1.0,\ L_x = 1.0,\ , L_y = 0.5,\ m = 1,\ n = 1,\ g = 1,\ f = 3.193379349.$

B.3 Poincaré wave in a circular basin

The Poincaré wave in a circular basin of radius R is given

$$\begin{aligned} u_r(r,\theta,t) &= \frac{gA}{f^2-\omega^2}(-\frac{m}{r}(f+\omega)\mathrm{F}_m(kr)+\omega k\mathrm{F}_{m+1}(kr))\cos(m\theta+\omega t),\\ u_\theta(r,\theta,t) &= \frac{gA}{f^2-\omega^2}(\frac{\omega m}{r}(f+\omega)\mathrm{F}_m(kr)-fk\omega k\mathrm{F}_{m+1}(kr))\sin(m\theta+\omega t),\\ \eta(r,\theta,t) &= H+A\mathrm{F}_m(kr)\sin(m\theta+\omega t) \end{aligned} \tag{B.4}$$

with $a^2=gH$, the solid wall boundary conditions at $r=R$. $\mathrm{F}_m(z)=J_m(z)$ are Bessel functions of the first kind, $\omega^2=f^2+a^2k^2$ is the dispersion relation and the wave number k has to satisfy the following relations due to the solid wall boundary conditions at $r=R$:

$$fm\mathrm{F}_m(kR)+wk\mathrm{F}_{m+1}(kR)=0.$$

The parameters are the following: $A=0.01,\ H=1.0,\ R=1,\ k=8.55806886,\ m=1,\ n=1,\ g=1,\ f=1.596689674$.

C Linear waves in closed parabolic bowl

¿From the solution in [8] (§193), we take the following case with $\alpha=n=s+4$, $\mathsf{i}^2=-1$ and in our notation $\zeta=\eta$, to obtain the following solution in polar coordinates

$$\eta(r,\theta,t)=A_s\left(\frac{r}{a}\right)^s\left(1-\frac{(s+2)}{(s+1)}\left(\frac{r}{a}\right)^2\right)e^{\mathsf{i}(\sigma t+s\theta)}, \tag{C.1a}$$

$$u_r(r,\theta,t)=\frac{g\,\mathsf{i}}{\sigma\,a}A_s\left(\frac{r}{a}\right)^{s-1}\left(s-\frac{(s+2)^2}{(s+1)}\left(\frac{r}{a}\right)^2\right)e^{\mathsf{i}(\sigma t+s\theta)}, \tag{C.1b}$$

$$u_\theta(r,\theta,t)=-\frac{g\,s}{\sigma\,r}A_s\left(\frac{r}{a}\right)^s\left(1-\frac{(s+2)}{(s+1)}\left(\frac{r}{a}\right)^2\right)e^{\mathsf{i}(\sigma t+s\theta)} \tag{C.1c}$$

with s a positive integer and

$$R=a\sqrt{\frac{s\,(s+1)}{(s+2)^2}}<a, \tag{C.2}$$

as required for linearity and positivity of $D(r)$, to satisfy the slip boundary condition $u(R,t)\propto\partial_r\eta|_{r=R}=0$. Furthermore, the rest depth is:

$$D(r)=D_0\left(1-r^2/a^2\right). \tag{C.3}$$

The real part of (C.1a) gives one of the desired modes

$$\eta(r,\theta,t) = A_s \left(\frac{r}{a}\right)^s \left(1 - \frac{(s+2)}{(s+1)}\left(\frac{r}{a}\right)^2\right) \cos(\sigma\, t + s\,\theta), \tag{C.4a}$$

$$u_r(r,\theta,t) = -\frac{g}{\sigma\, a} A_s \left(\frac{r}{a}\right)^{s-1} \left(s - \frac{(s+2)^2}{(s+1)}\left(\frac{r}{a}\right)^2\right) \sin(\sigma\, t + s\,\theta), \tag{C.4b}$$

$$u_\theta(r,\theta,t) = -\frac{g\, s}{\sigma\, r} A_s \left(\frac{r}{a}\right)^s \left(1 - \frac{(s+2)}{(s+1)}\left(\frac{r}{a}\right)^2\right) \cos(\sigma\, t + s\,\theta). \tag{C.4c}$$

The frequency for the case $\alpha = n = s + 4$ is given by

$$\sigma^2 = g\, D_0\, (6\, s + 8)/a^2. \tag{C.5}$$

The parameter values are: $s = 2,\ A_s = 0.1,\ D_0 = 1,\ R = 1,\ g = 1,\ a = R\sqrt{(s+2)^2/[s(s+1)]}$.

D Exact solution of the Maxwell equations

The smooth exact solution of the Maxwell equation (5.1) is

$$\begin{pmatrix} H_x \\ H_y \\ E_z \end{pmatrix} = \begin{pmatrix} -\beta \\ \alpha \\ 1 \end{pmatrix} \exp(\cos(\alpha x + \beta y + t)). \tag{D.1}$$

The solution with a singularity in equation (5.1) is

$$\begin{pmatrix} H_x \\ H_y \\ E_z \end{pmatrix} = \begin{pmatrix} -\beta \\ \alpha \\ 1 \end{pmatrix} \varphi((\cos(\alpha x + \beta y + t))), \tag{D.2a}$$

$$\varphi(w) = \begin{cases} w \log|w|, & \text{if } w \neq 0 \\ 0, & \text{if } w = 0 \end{cases}, \tag{D.2b}$$

where $\alpha = \cos(0.3\pi)$ and $\beta = \sin(0.3\pi)$.

References

[1] O. Bokhove and M. Oliver, *Parcel Eulerian-Lagrangian fluid dynamics for rotating geophysical flows,* Proc. Roy. Soc. A. **462** (2006), 2563–2573.

[2] C. Blom, *Discontinuous Galerkin method on tetrahedral elements for aeroacoustic.* Ph.D. Thesis, University of Twente, Enschede, The Netherlands, (2003).

[3] B. Cockburn, S. Hou and C.-W. Shu, *The Runge-Kutta local projection discontinuous Galerkin finite element method for conservation laws IV: the multidimensional case*, Math. Comp., **54** (1990), pp.545–581.

[4] B. Cockburn and C.-W. Shu, *The Runge-Kutta discontinuous Galerkin method for conservation laws V: multidimensional systems*, J. Comput. Phys., **141** (1998), pp.199–224.

[5] E. Hairer, C. Lubich and G. Wanner, Geometric numerical integration: structure preserving algorithms for ordinary differential equations. Springer, Heidelberg (2002).

[6] E. Hairer, C. Lubich and G. Wanner, *Geometric numerical integration illustrated by the Störmer-Verlet method*, Acta Numerica, **12** (2003), pp.399–450.

[7] T. Huttunen, P. Monk, F. Collino and J.P. Kaipio, *The ultra-weak variational formulation for elastic wave problems,* SIAM J. Sci. Comput., **25** (2004), pp.1717–1742.

[8] H. Lamb, *Hydrodynamics*, sixth edition, Cambridge University Press, London, 1975.

[9] J. Lighthill, *Waves in fluids*, Cambridge University Press, London, 1978.

[10] J.E. Marsden and T.S. Ratiu, Introduction to mechanics and symmetry, A basic exposition of classical mechanical systems. Texts in Applied Mathematics, 17. Springer-Verlag, New York, 1994.

[11] P.J. Morrison, *Hamiltonian description of the ideal fluid*, Reviews of Modern Physics, **70** (1998), pp.467–521.

[12] R. Salmon, *Lectures on geophysical fluid dynamics*, Oxford University Press (1998).

[13] C.-W. Shu and S. Osher, *Efficient implementation of essentially non-oscillatory shock-capturing schemes*, J. Comput. Phys., **77** (1988), pp.439–471.

[14] J. Yan and C.-W. Shu, *Local discontinuous Galerkin methods for partial differential equations with higher order derivatives*, J. Sci. Comp., **17** (2002), pp.27–47.